

Self-assembled π -conjugated organic nanoplates: from hexagonal to triangular motifs.

Daniel E. Martínez-Tong^{†,*}, Gabin Gbabode[∇], Christian Ruzié[‡], Basab Chattopadhyay[‡], Guillaume Schweicher^{‡,▲}, Alan R. Kennedy[†], Yves H. Geerts[‡], Michele Sferrazza[†]

[†]Département de Physique, Faculté des Sciences, Université Libre de Bruxelles, 1050 Brussels, Belgium

[∇]Normandie Université, Laboratoire SMS EA 3233, Université de Rouen, F-76821 Mont Saint Aignan, France

[‡]Laboratoire de Chimie des Polymères, Faculté des Sciences, Université Libre de Bruxelles, 1050 Brussels, Belgium

[†]Department of Pure and Applied Chemistry, University of Strathclyde. 295 Cathedral Street, Glasgow G1 1XL, Scotland

*Corresponding author: danmarti@ulb.ac.be

[▲]Present address: Optoelectronics Group, Cavendish Laboratory, University of Cambridge, JJ Thomson Avenue, Cambridge CB3 0HE, UK

Abstract

Organic semiconducting materials in confined geometries present interesting properties connected to change or coexistence of molecular organizations, depending on their characteristic scales. In this work the preparation and structural characterization of self-assembled π -conjugated organic nanoplates of 2,7-diperfluorohexyl-[1]benzothieno[3,2,b]benzothiophene are studied. These nanostructures were prepared by spin coating, implementing a fast precipitation method. We observed an evolution of the nanostructures from hexagonal towards triangular nanoplates, possibly driven by enhanced solvent/molecule interactions, and accompanied by the formation of a new polymorph.

Introduction

Current interest in developing organic-based technologies requires an understanding and control of the molecular organization of materials at the nanoscale. At this scale, different structural phases can be observed and a study of the organization of the first monolayers of organic materials is then crucial to better understanding the properties under confinement.¹⁻³ For example, charge transport properties have been shown to be influenced by the molecular organization of lateral domains at the interfacial level of the first molecular layers.^{4,5}

Among confined geometries, special attention has been drawn towards two-dimensional materials, *i. e.* systems where only one of its geometrical dimensions is in the nanoscale regime, having thus large specific surface areas.⁶ One issue that is relevant when transitioning from bulk towards a confined level is related to the structural organization of the molecules. By decreasing the characteristic thickness, it has been observed a change of the crystal organization compared to the bulk one⁷ or a coexistence of crystalline phases⁸ (polymorphism). The crystal structure of the material may also evolve depending on different parameters, such as thickness, aging of the film or solvent annealing, tuning then the crystal organization from metastable phases to thermodynamically stable phases.^{3,9}

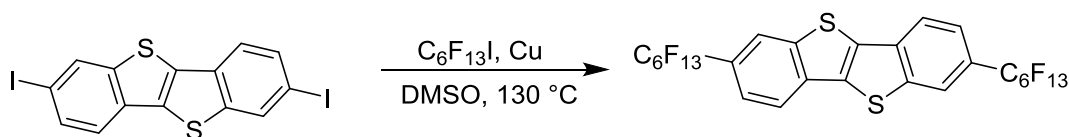
Soft materials are the subject of intense research due to their self-assembly properties, structural control and flexibility, diversity of fabrication approaches, etc.⁶ In this area, it is possible to find bidimensional systems such as *nanoplates*: materials which are typically nanoscale in one dimension, yet microscale in the other two,¹⁰⁻¹² and that, contrary to thin films, do not span large surface areas but are distributed as features, generally on a supporting substrate. The idea behind nanoplates consists in developing independent nanostructures with well controlled and tunable geometries,¹³ such as squares,¹⁴ hexagons¹⁵ and triangles,¹⁶ which could lead to different specific applications in organic-based technologies. For example, it is possible to prepare nanoplates of organic molecules with a π -conjugated (hetero)aromatic backbone.¹⁷ Typically, these structures are stabilized by the π - π interactions within self-assembled stacked lamellae^{1,2} which in turn provide anisotropic channels for the transportation of charge carriers and efficient light interaction.¹³ Following these ideas, in this work we present the

preparation and structural characterization of self-assembled π -conjugated organic nanoplates of 2,7-diperfluorohexyl-[1]benzothieno[3,2,*b*]benzothiophene ($F_{13}C_6$ -BTBT- C_6F_{13}). By means of a fast precipitation protocol we have prepared different nanostructures, by changing the solution concentration. We observed an evolution from hexagonal nanoplates towards equilateral triangles which lead to a change in the crystalline structure of the material.

Experimental

2,7-Diperfluorohexyl-[1]benzothieno[3,2,*b*]benzothiophene ($F_{13}C_6$ -BTBT- C_6F_{13}) synthesis.

All reagents and solvents were purchased from Aldrich, Alfa Aesar, or Acros. 2,7-diiodo-[1]benzothieno[3,2-*b*][1]benzothiophene ($F_{13}C_6$ -BTBT- C_6F_{13}) has been synthesized according to known procedures¹⁸.



A mixture of 2,7-diiodo-[1]benzothieno[3,2-*b*][1]benzothiophene (492 mg, 1 mmol), Cu powder (572 mg, 9 mmol), and perfluorohexyliodide (1.08 mL, 5 mmol) in anhydrous DMSO (20 mL) in a Schlenk flask was degassed by 2 “freeze-pump-thaw” cycles. The Schlenk flask was filled with Ar, and sealed. The mixture was heated for 2 days at 130 °C. After cooling to room temperature, water (50 mL) was added. The resulting precipitate was filtrated, washed with water, and methanol. The dried residue was dissolved in boiling tetrachloroethane and subjected to short silica filtration to afford after evaporation and recrystallization in tetrachloroethane a white powder (682 mg, 78 %). ¹H NMR (400 MHz, C₂D₂C₁₄, 363 K) δ = 8.26 (s, 2H), 8.10 (d, *J*=8.1 Hz, 2H), 7.75 (dd, *J*=8.1 and 2.1 Hz, 2H); ¹⁹F NMR (376 MHz, C₂D₂C₁₄, 363 K) δ = -81.3 (m, 3F), -109.6 (m, 2F), -121.5 (m, 4F), -122.9 (m, 2F), -126.2 (m, 2F). HRMS (MALDI-HRMS): *m/z* calculated for C₂₆H₆F₂₆S₂: 875.9496; found 875.9468.

Single-Crystal X-ray Diffraction. Single-Crystal data was measured at 123(2) K with an Oxford Diffraction Gemini S diffractometer using CuK α radiation (λ = 1.5418 Å). The crystal structure was solved by direct methods using SHELXS and refined by full

matrix least-squares methods based on F^2 using SHELXL97.¹⁹ The displacement parameters of all non-H-atoms were treated anisotropically. H-atoms were placed at calculated positions using suitable riding models with fixed isotropic thermal parameters [$U_{\text{iso}}(\text{H})=1.2U_{\text{eqv}}(\text{C})$ for CH groups]. The thermal displacement parameters for the terminal CF_3 group required restraints to be applied before a sensible model was obtained. Crystal data for $\text{F}_{13}\text{C}_6\text{-BTBT-C}_6\text{F}_{13}$ are summarized in table 1 and full details are available in cif format. Molecular view is given in Figure 1.

Table 1. Crystal data for compound $\text{F}_{13}\text{C}_6\text{-BTBT-C}_6\text{F}_{13}$.

	$\text{F}_{13}\text{C}_6\text{-BTBT-C}_6\text{F}_{13}$
Empirical formula	$\text{C}_{26}\text{H}_6\text{F}_{26}\text{S}_2$
Formula weight	876.43 Da
Crystal system	Monoclinic
Space group	$C2/c$
a, b, c [Å]	53.119(8) 5.8356(6) 9.0022(13)
β [°]	95.343(15)
Volume [Å ³]	2778.4(6)
Z, Z'	4, 0.5
Density [g cm ⁻³]	2.095
Crystal size [mm ³]	0.12 x 0.10 x 0.03
Reflections collected	9621
Independent reflections	2742, [R(int) = 0.0682]
Goodness-of-fit on F^2	1.080
Final R indices [I > 2σ(I)]	R1 = 0.0628, wR2 = 0.1630
R indices (all data)	R1 = 0.0995, wR2 = 0.2022

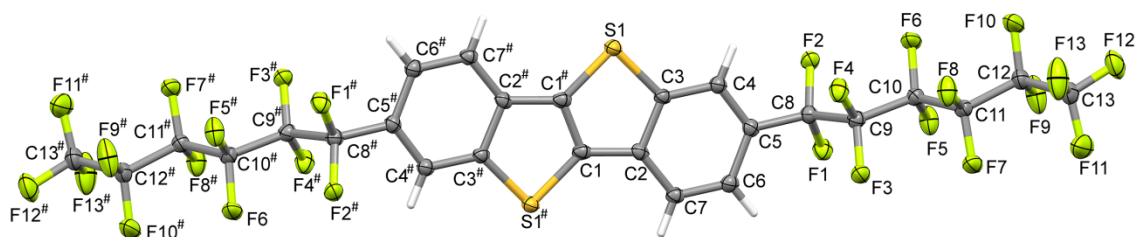


Figure 1. Molecular view of $F_{13}C_6$ -BTBT- C_6F_{13} . The atoms marked with # are generated by symmetry.

Hirshfeld Surfaces^{20, 21} and the associated fingerprint plots²² were calculated using Crystal Explorer²³ which accepts a structure input file in the CIF format. Bond lengths to hydrogen atoms were set to typical neutron values (C-H=1.083 Å). For each point on the Hirshfeld isosurface, two distances d_e , the distance from the point to the nearest nucleus external to the surface, and d_i , the distance to the nearest nucleus internal to the surface, are defined. The normalized contact distance (d_{norm}) based on d_e and d_i is given by:

$$d_{\text{norm}} = \frac{(d_i - r_i^{\text{vdW}})}{r_i^{\text{vdW}}} + \frac{(d_e - r_e^{\text{vdW}})}{r_e^{\text{vdW}}}$$

where r_i^{vdW} and r_e^{vdW} are the van der Waals radii of the atoms. The value of d_{norm} is negative or positive depending if the intermolecular contacts are shorter or longer than the van der Waals separations. The parameter d_{norm} displays a surface with a red-white-blue color scheme, where bright red spots highlight shorter contacts, white areas represent contacts around the van der Waals separation, and blue regions are devoid of close contacts.

Nanoplates preparation. A 10 mg/mL solution of $F_{13}C_6$ -BTBT- C_6F_{13} in trifluorotoluene (α,α,α -TFT, Sigma Aldrich, boiling point: 103 °C) was prepared. Complete dissolution was achieved by heating the mixture at 90 °C for 1 hour, under continuous stirring on a hot plate. We have observed a fully transparent solution with a lack of coloration of the mixture after 15 min. If the solution was allowed to cool down, precipitation of the solid phase occurs when temperature reached values below 50 °C. This allowed to form microscopic hexagonal and needle-shaped structures dispersed in the TFT (bulk crystallization), and the whole system becomes a white-colored emulsion. Thus, considering the facile precipitation of the solid, we have implemented a fast

precipitation strategy, in order to avoid macroscopic aggregation and allow the preparation of nanocrystals. In this protocol, after achieving dissolution, the solution's temperature was raised up to 100 °C and immediately deposited onto (100) silicon wafers by spin coating (3000 rpm, 1 min). From the 10 mg/mL master solution, several diluted concentrations (5, 1 and 0.25 mg/mL) were prepared by adding TFT and repeating the heating and deposition protocol.

Atomic Force Microscopy (AFM). A Multimode microscope, equipped with a Nanoscope IIIa controller (Bruker), under tapping protocol was used (NSC14 probes, μ Marsch, resonant frequency \approx 150 kHz). 512x512 pixels resolution images were taken. Analysis of size and shape of the nanometric features was performed with the NanoScope Analysis 1.50 software (Bruker).

X-ray Measurements. Specular X-ray diffraction (sXRD) measurements were carried out on a Bruker D8 Advance diffractometer, using $\text{CuK}\alpha$ radiation ($\lambda = 1.5418 \text{ \AA}$). This technique measures the lattice spacing perpendicular to the plane of the substrate. Diffraction patterns were collected in the scattered angular range between 3° and 45°, with an angular resolution of 0.01° and a typical counting time of 20 s per step, using the θ/θ reflection geometry (the source and detector both move from the horizontal sample plane at the same angle θ , that is, in specular reflection condition). All sXRD patterns are presented as the scattering intensity (in counts) versus q (in nm^{-1}), the scattering vector, defined as $q = 4\pi/\lambda \sin \theta$.

Crystal growth morphology calculations. The crystal growth morphology of $\text{F}_{13}\text{C}_6\text{-BTBT-C}_6\text{F}_{13}$ has been modeled from the crystal structure determined by single crystal X-ray diffraction using the Morphology module of the Materials Studio package²⁴. The attachment energy (E_{att}) method developed by Hartman²⁵⁻²⁷ has been performed to determine the relative importance of the different crystallographic faces in the crystal morphology: globally, faces with higher E_{att} (in absolute value) grow faster and have then less importance in the final crystal shape and vice versa. E_{att} are explicitly calculated for each crystal face from the crystal structure using Compass forcefield²⁸ with an accuracy lower than 1 kJ/mol.

Results and discussion

Crystal structure analysis. Single crystals of $F_{13}C_6$ -BTBT- C_6F_{13} were grown from 1,2,4-trichlorobenzene solution. $F_{13}C_6$ -BTBT- C_6F_{13} crystallizes in a monoclinic unit cell with space group $C2/c$ with the asymmetric unit consisting of half of the molecule, *i.e.* $Z' = 0.5$. The fluorination of the alkyl side chains leads to an orthogonal orientation with respect to the planar BTBT core; the torsion angle between the first two C atoms of the alkyl chain and C atoms of the aromatic ring (C4C5C8C9) adopts a value of $91.1(5)^\circ$. The value of the corresponding torsion angle in non-fluorinated C8-BTBT²⁹ is $65.7(7)^\circ$. The crystal structure of $F_{13}C_6$ -BTBT- C_6F_{13} can be best described as a “layer-by-layer” organization with the molecules in each layer packed in a herringbone motif stabilized by C-H $\cdots\pi$ interactions (Figures 2 and 3). The herringbone packing is also observed in unsubstituted BTBT³⁰ as well as in the non-fluorinated C8-BTBT.²⁹ Additional reinforcements in form of intermolecular C-H \cdots F and F \cdots F interactions stabilize the lamellar herringbone layer (Figure 2a).

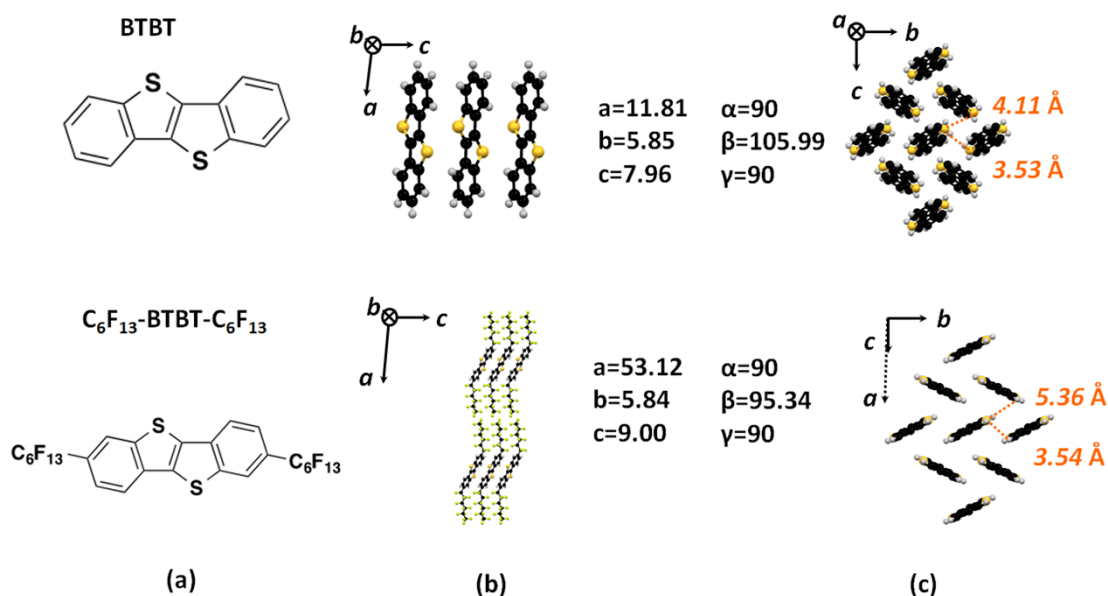


Figure 2. a) Molecular structure of $F_{13}C_6$ -BTBT- C_6F_{13} along with the unsubstituted BTBT³⁰ is presented for comparison. b) Side view of the crystal packing. c) Lattice parameters and top view of the lamellar herringbone packing structure.

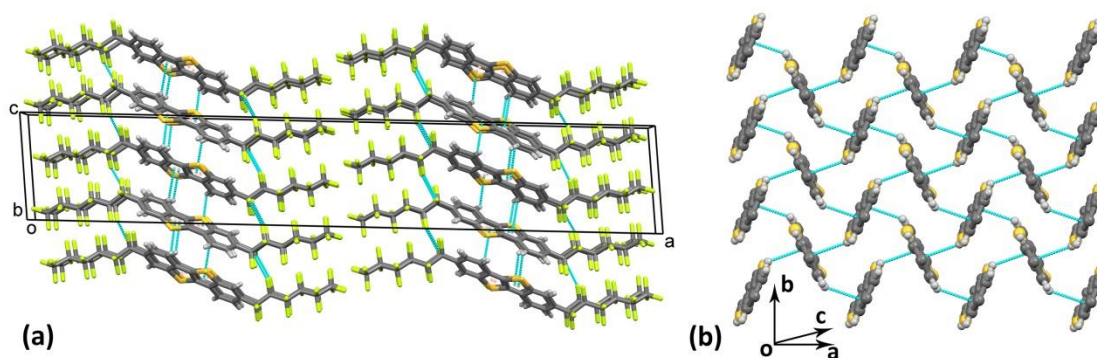


Figure 3. a) Perspective view of the crystal packing of $F_{13}C_6$ -BTBT- C_6F_{13} along crystallographic b -axis. $C-H \cdots \pi$ and $F \cdots F$ interactions are shown. b) View of the herringbone packing structure formed via $C-H \cdots \pi$ interactions. Terminal C_6F_{13} chains are not shown for clarity.

In order to have a clear quantitative and visual insight of the intermolecular interactions, the Hirshfeld surfaces of the unsubstituted BTBT, C_8 -BTBT- C_8 and $F_{13}C_6$ -BTBT- C_6F_{13} is presented in Figure S1 (supplementary material) showing surfaces that have been mapped over a d_{norm} range of -0.5 to 1.5 Å. The dominant interactions can be seen in the Hirshfeld surfaces (Figure S1) as the bright red areas corresponding to the $C-H \cdots \pi$ interactions, and $C-H \cdots F$ and $F \cdots F$ contacts in $F_{13}C_6$ -BTBT- C_6F_{13} . A look at the 2D fingerprint plots (Figure 4a) reveals that fluorination of the alkyl side chains leads to a different packing environment although all three compounds exhibit a similar herringbone motif. The $C-H \cdots \pi$ hydrogen bonds in the unsubstituted BTBT, C_8 -BTBT- C_8 and $F_{13}C_6$ -BTBT- C_6F_{13} are well manifested and appear as a pair of wings of almost equal lengths in the (d_i, d_e) regions (1.7 Å, 1.1 Å) and (1.1 Å, 1.7 Å). For $F_{13}C_6$ -BTBT- C_6F_{13} , the $C-H \cdots F$ interactions appear as sharp spikes in the (d_i, d_e) regions (1.4 Å, 1.1 Å) and (1.1 Å, 1.4 Å). Moreover, the $F \cdots F$ interactions in $F_{13}C_6$ -BTBT- C_6F_{13} contributes to the spike at $d_i = d_e = 1.4$ Å. This is in contrast to the unsubstituted BTBT and C_8 -BTBT- C_8 where the spike at $d_i = d_e = 1.2$ Å is a consequence of the short intermolecular $H \cdots H$ contacts. Figure 4b highlights the relative contributions of different intermolecular interactions to the Hirshfeld surface area. The quantitative analysis shows that $C \cdots H$ contacts corresponding to $C-H \cdots \pi$ interactions account for 35.3% in the unsubstituted BTBT and 14.9% in C_8 -BTBT- C_8 while in $F_{13}C_6$ -BTBT- C_6F_{13} it is only 12.3% of the Hirshfeld surface area. In $F_{13}C_6$ -BTBT- C_6F_{13} the absence of hydrogen atoms among the lateral chains reduces considerably the impact of the hydrogen interactions and leads to a packing dominated by fluorine interactions as can be observed by the drastic decrease of the $H \cdots H$ and $C \cdots H$ interactions (15.4 % in total) and huge contributions of the $F \cdots F$, $F \cdots C$ and $F \cdots H$ interactions (71.6 % in total).

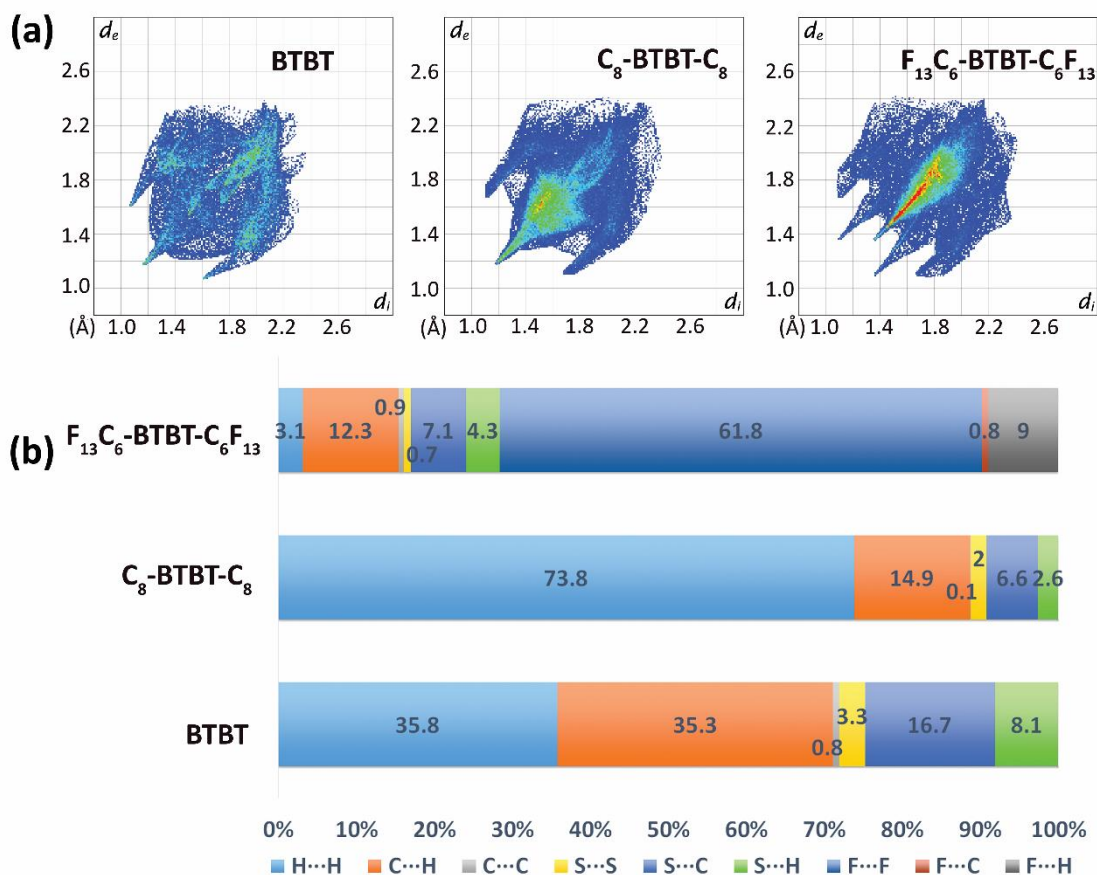


Figure 4. a) Fingerprint plots and b) relative contributions to the Hirshfeld surface areas for the various intermolecular contacts for BTBT core, C₈-BTBT-C₈ and F₁₃C₆-BTBT-C₆F₁₃.

Self-assembled nanoplates. Figure 5 shows AFM height images of the deposited samples for different solution concentrations. For all the concentrations, we observe a distribution of different geometrical features, as well as the development of nanoplates with different molecular organizations. The appearance of a geometrical distribution, can be related to the way the solid precipitates during spin coating: areas with higher accumulation of material allow nucleation and growth of bigger motifs, while as material gets depleted lower dimensional structures are formed due to fewer nucleation sites. Moreover, for the lower concentration a triangular shape nanoplate is observed.

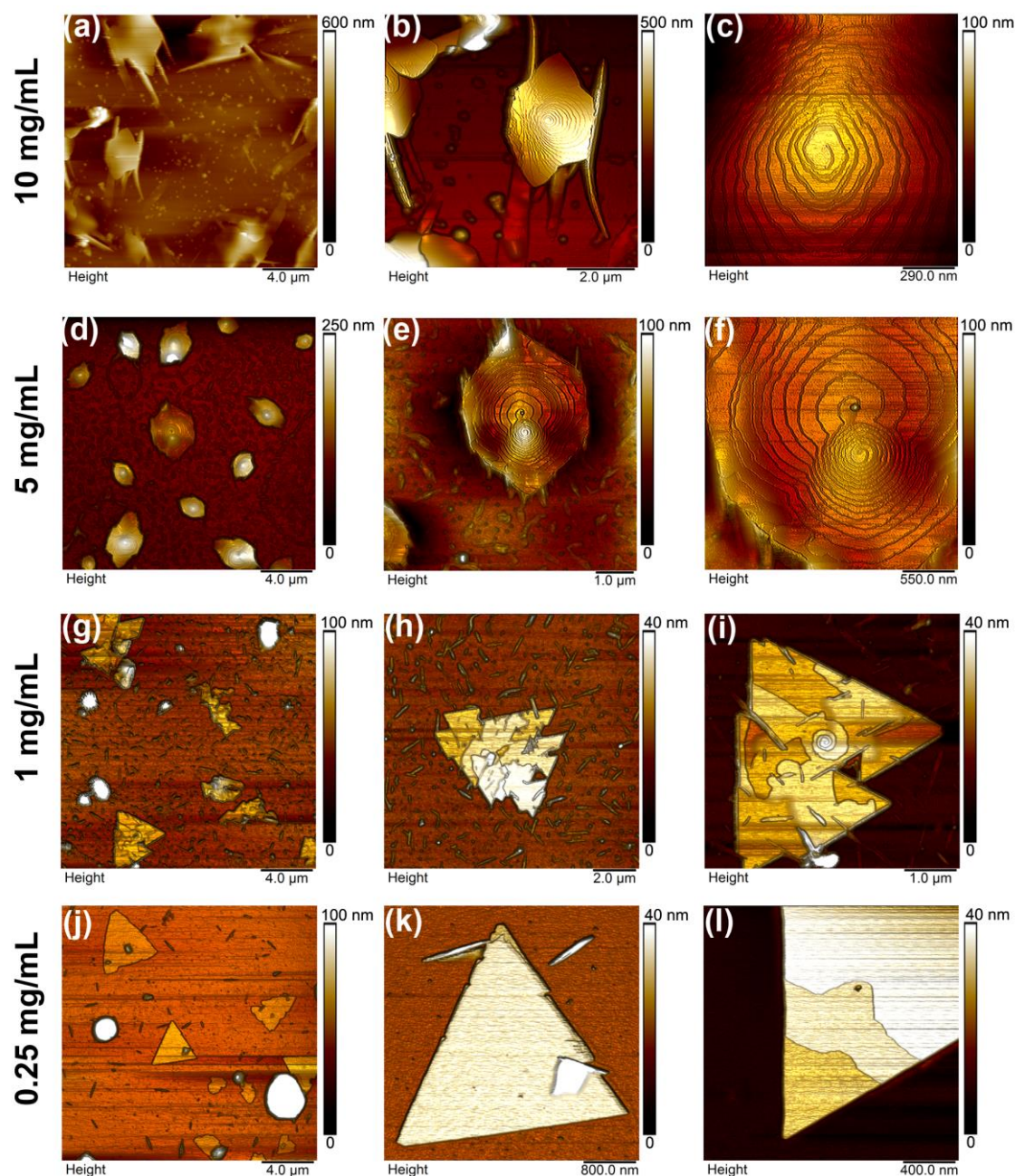


Figure 5. AFM tapping height images of the prepared samples. For each row, we present scans in decreasing size, from left to right, in order to allow evidencing the different length scales of the molecular arrangements.

Concentrated samples (10 mg/mL and 5 mg/mL) show the development of polygonal nanoplates randomly distributed on the silicon surface. Specifically, in Figure 5a, the 10 mg/mL preparation shows features spanning areas around $5 \mu\text{m}^2$ and having heights from 200 – 500 nm (at their highest point, respect to the silicon). In most of the cases, these features have 5, 6 to 8 lateral sides, mostly resembling the general shape of hexagons. Also, we observe elongated walls apparently emerging from the edge of the nanoplates, as shown in Figure 5b. These features are likely related to possible vestiges

of the nanoplates' formation process. As solution concentration was decreased to 5 mg/mL, changes in the shape and size of the molecular organization are observed. In this case several structures show a (almost) hexagonal geometry, with areas between 1-2 μm^2 and heights close to 200 nm (please refer to Figure 5d). The transition toward more defined structures, as well as the decrease in their characteristics dimensions, can be related to the availability of material at this concentration: as solution gets diluted, less material can be processed into the final nanostructures.

Considering the bulk crystal structure presented in the previous section, we have calculated the expected crystal growth morphology using the *Morphology* module implemented in Materials Studio software (see Experimental Section). In consistency with the AFM observations, the calculated morphology is octagonal (see Figure S2) with the large top and bottom surfaces corresponding to the {200} faces, that is, with the molecular axis perpendicular to these faces. However, hexagonal shaped crystals are more observed by AFM. This is not really an inconsistency with the calculation, as the latter does not take into account solvent-solute interactions that might inhibit the growth of certain crystal faces,¹⁶ resulting in an observed crystal morphology slightly different from the theoretical one. For example, if we suppose that the {110} or {002} faces are totally absent from the theoretical morphology, we will end up with a hexagonal crystal morphology akin to that observed by AFM. The relevant data from the calculations are gathered in table 2. There we present the interreticular distance (d_{hkl}) of the (hkl) reticular planes and the attachment energy (E_{att}) and facet coverage percentage of the corresponding {hkl} crystal faces.³¹ The lower the attachment energy of a given face (in absolute values), the lower is its growth rate and consequently the higher should be its area in the final crystal morphology.

Table 2. Attachment energy and corresponding percentage of total facet area of the most dominant faces in the calculated crystal morphology of $\text{F}_{13}\text{C}_6\text{-BTBT-C}_6\text{F}_{13}$.

hkl	d_{hkl} (Å)	E_{att} (kJ/mol)	% Total facet area
{2 0 0}	26.4	-17	78.0
{1 1 1}	4.8	-118	9.3
{0 0 2}	4.5	-135	5.7
{1 1 0}	5.8	-116	4.3
{1 1 -1}	4.9	-121	2.7

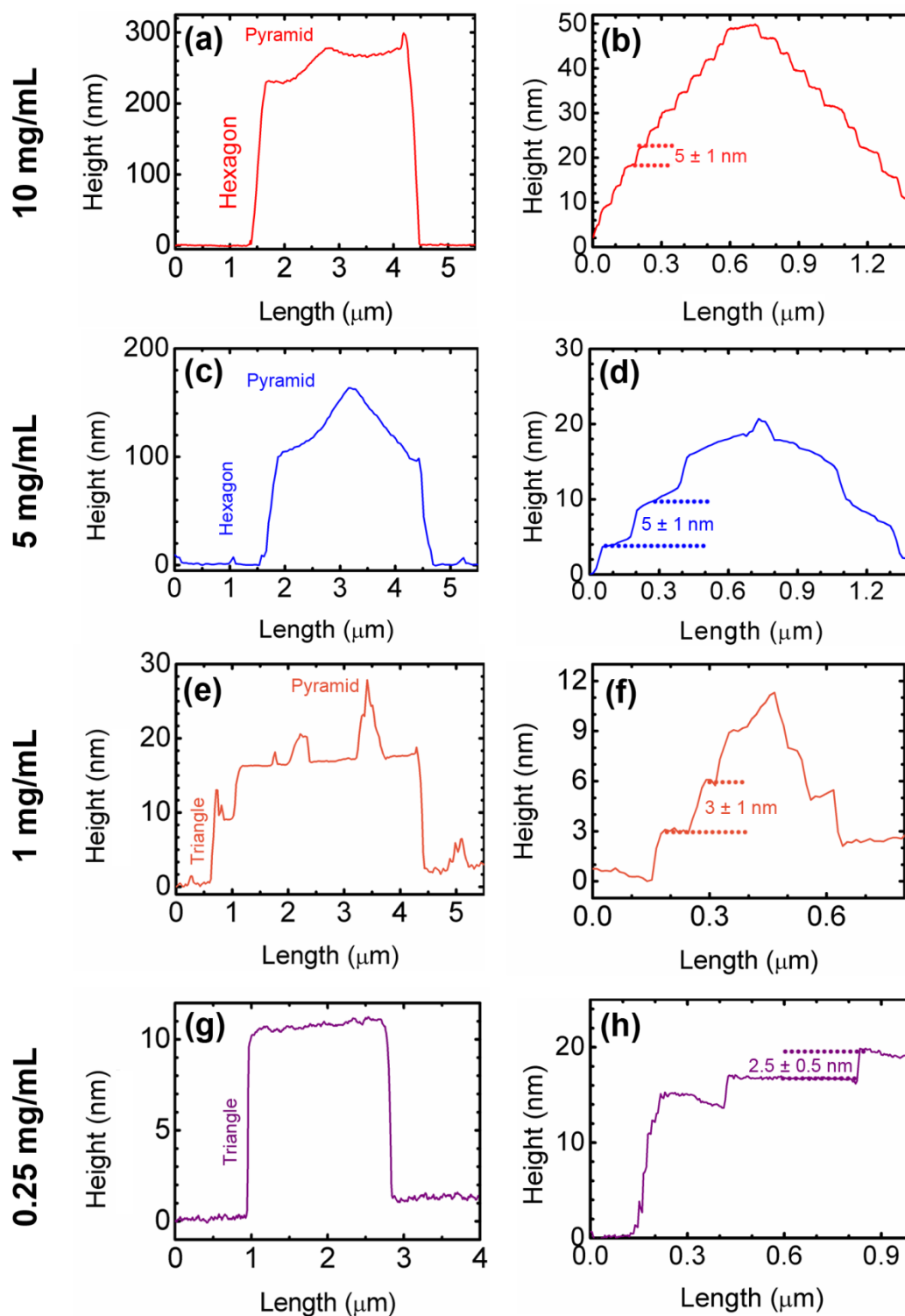


Figure 6. Height profiles of selected AFM tapping height images. Left column shows the general outlook of the nanoplates, while in the right column we present the terraces layout, and the characteristic step size.

We have performed AFM scans on the top surface of the nanoplates, presented in Figures 5c and 5f. Here, it is possible to observe the development of spiral staircase-like structures, formed by the arrangement of step-distributed terraces, with cores at the center of the nanoplates. As detailed in Figure 5f, the spirals can grow either left- or

right-handed, and more than one core might exist within the same surface. As previously reported for other nanostructures with comparable geometries,¹⁰ our nanoplates show interference patterns when the sample is illuminated under simple bright-field optical microscopy, revealing the geometry and thickness variation of the nanoplate, and the location of the core (Figure S3). The layout of spiral staircase-like structures has been previously observed in inorganic^{10, 32} and organic^{33, 34} materials, and was originally discussed by Burton-Cabrera-Frank³⁵ (BCF) to describe the crystal growth from vapors and solutions at low supersaturations, near equilibrium.^{32, 36} Based on the concept of screw dislocations, introduced previously by Frank,³⁷ the BCF theory states that the sources of surface steps is related to the presence of imperfections (dislocations) in their lattice. When dislocations have a screw component, the existence of steps on the surface would be assured during growth, obviating the necessity of surface nucleation.³⁸ Growth would occur by the incorporation of molecules into steps disposed in spirals, in a self-perpetuating process: if a screw dislocation intercepts a closely packed face, there forms on the face a spiral step that serves as a permanent source of growth layers.^{36, 38}

AFM height profiles are shown in Figure 6. Particularly, Figure 6a shows the profile of the hexagonal structure of Figure 5b. Starting from the left side of the Figure, we observe the hexagon edge emerging from the Si substrate up to a ≈ 230 nm height. Then, on top of the hexagon the profile is not flat, but a pyramid-like structure is depicted, corresponding to the molecular spiral staircase. As shown in Figure 6b, this upper feature has a height of 55 ± 2 nm (measured from the base of the hexagon), and is made out of steps of $h = 5 \pm 1$ nm in height and widths of variable length from 20 to 80 nm. On the other hand, Figures 6c and 6d show the lateral profile of a hexagon prepared from the 5 mg/mL sample. As in the previous case, in Figure 6c one can observe the edge of the hexagon raising from the substrate up to a height close to 100 nm, while on top of the hexagon, the pyramid profile of the spiral arrangement is also evidenced. The total height of the pyramid is around 60 ± 1 nm, while the step layout shows a mean height of 5 ± 1 nm per step, just like the one found at the 10 mg/mL preparation. If one compares the step height of the spirals with the crystalline dimensions of the molecule (see Methods), we observe that the step-height value of 5 nm, found by AFM, is fairly similar to the size of a bilayer along the *a* axis (~ 5.3 nm) of the monoclinic unit cell. Thus we can assume that the nanoplates' terraces are formed by layers stacked in the

[100] direction. In order to further explore this hypothesis, we have performed specular X-ray Diffraction (sXRD) measurements.

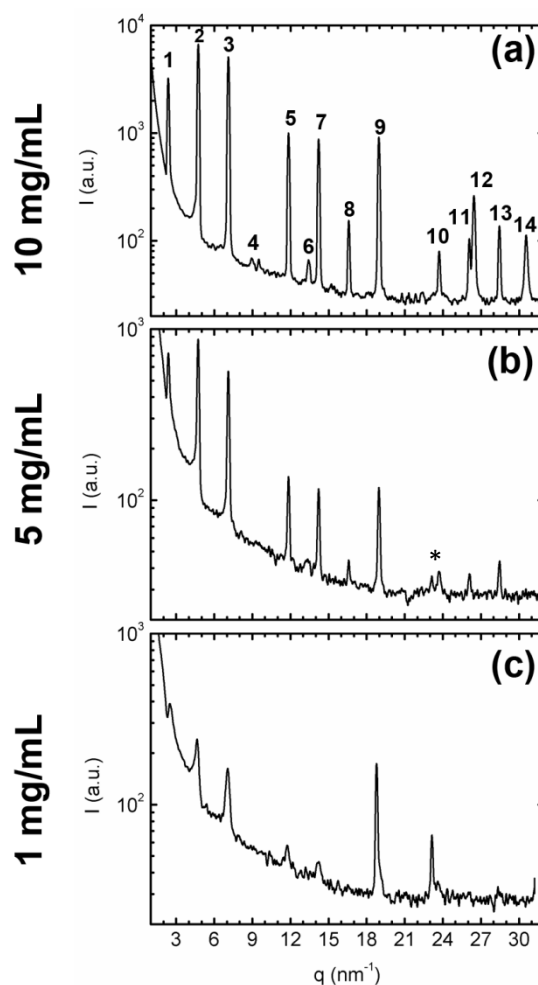


Figure 7. Specular X-ray Diffraction (sXRD) patterns of the prepared samples, showing diffracted intensity as a function of the scattering vector q . Numbered labels in (a) serve as guide for the indexing presented in table 1. The asterisk indicates the position of the 100 reflection coming from the Si wafer.

Figures 7a and 7b show the diffraction patterns for the 10 mg/mL and 5 mg/mL samples, respectively. In both cases, several sharp diffraction peaks are observed, indicating that in both samples the nanoplates consist of crystalline material. The q -positions of the peaks' maxima are summarized in table 3, and have been indexed considering the monoclinic crystal structure of the unit cell. Comparing between these two preparations, no displacements on the peaks' positions are observed: nanoplates are formed by the same crystalline arrangement of the molecules. The only appreciable variation is the decrease of the peaks' intensity, which can be related to the smaller size

and the lower number of the 5 mg/mL nanostructures, as observed by AFM. Indexation shows that, in both cases, most of the peaks correspond to $h00$ reflections, with the particularity of $h = \text{even}$ as expected from the extinction conditions related to a $C2/c$ space group. In combination with higher order reflections, in Figures 7a and 7b it is possible to estimate an out-of-plane lattice spacing close to 53 Å, fairly comparable to the 53.1 ± 0.1 Å of the unit cell crystal structure, and thus suggesting a preferential upright standing orientation of the molecules in the nanoplates, as previously discussed by comparing with the AFM results and also consistently with the calculated crystal morphology shown in supporting information. Finally, for both preparations, reflections related to the molecular packing within the lamellae can be observed for $q > 13 \text{ nm}^{-1}$ between the $h00$ peaks (see also table 3), similar to previous reports for other BTBT derivatives.²

Table 3. q -position (nm^{-1}) and indexing of the sXRD peaks shown in Figure 6. The error associated to each maximum is the half width at half maximum of the corresponding peak.

Label (see Figure 7)	10 mg/mL	5 mg/mL	1 mg/mL	Index <i>Monoclinic</i>	Index <i>Hexagonal</i>
1	$2.36 \pm 0.05 \text{ nm}^{-1}$	$2.38 \pm 0.05 \text{ nm}^{-1}$	$2.51 \pm 0.07 \text{ nm}^{-1}$	2 0 0	0 0 1
2	$4.73 \pm 0.07 \text{ nm}^{-1}$	$4.73 \pm 0.07 \text{ nm}^{-1}$	$4.64 \pm 0.06 \text{ nm}^{-1}$	4 0 0	0 0 2
3	$7.10 \pm 0.06 \text{ nm}^{-1}$	$7.11 \pm 0.07 \text{ nm}^{-1}$	$7.05 \pm 0.07 \text{ nm}^{-1}$	6 0 0	0 0 3 0 1 1 1 0 1
4	$9.49 \pm 0.06 \text{ nm}^{-1}$	---	---	8 0 0	0 0 4
5	$11.84 \pm 0.06 \text{ nm}^{-1}$	$11.85 \pm 0.07 \text{ nm}^{-1}$	$11.75 \pm 0.08 \text{ nm}^{-1}$	10 0 0	0 0 5
6	$13.42 \pm 0.08 \text{ nm}^{-1}$	$13.3 \pm 0.3 \text{ nm}^{-1}$	---	3 1 1	2 0 1
7	$14.21 \pm 0.05 \text{ nm}^{-1}$	$14.22 \pm 0.06 \text{ nm}^{-1}$	$14.21 \pm 0.08 \text{ nm}^{-1}$	12 0 0	0 0 6
8	$16.58 \pm 0.06 \text{ nm}^{-1}$	$16.60 \pm 0.07 \text{ nm}^{-1}$	---	14 0 0	0 0 7
9	$18.95 \pm 0.06 \text{ nm}^{-1}$	$18.97 \pm 0.06 \text{ nm}^{-1}$	$18.78 \pm 0.06 \text{ nm}^{-1}$	16 0 0	0 0 8
Si Wafer (100)	---	$23.1 \pm 0.1 \text{ nm}^{-1}$			
10	$23.70 \pm 0.06 \text{ nm}^{-1}$	$23.7 \pm 0.5 \text{ nm}^{-1}$	$23.6 \pm 0.5 \text{ nm}^{-1}$	20 0 0	0 0 10
11	$26.07 \pm 0.06 \text{ nm}^{-1}$	$26.1 \pm 0.1 \text{ nm}^{-1}$	---	22 0 0	0 0 11
12	$26.43 \pm 0.06 \text{ nm}^{-1}$	---	---	22 0 -1	---
13	$28.44 \pm 0.06 \text{ nm}^{-1}$	$28.47 \pm 0.08 \text{ nm}^{-1}$	$28.4 \pm 0.1 \text{ nm}^{-1}$	24 0 0	0 0 12
14	$30.55 \pm 0.06 \text{ nm}^{-1}$	---	---	3 1 4	---

As shown in Figure 5, when the deposition process was performed with the 1 mg/mL solution, a sudden change in the nanoplates geometry took place (refer to Figures 5g, 5h and 5i, in comparison to the higher concentrations). Specifically, the hexagonal shape of the nanoplates evolved towards sharp-edged polygonal structures. The AFM images showed that these new geometries are formed by (*truncated*-) triangular nanoplates (Figures 5h and 5i), with an area distribution around $5 \pm 1 \mu\text{m}^2$ and heights close to $25 \pm 5 \text{ nm}$. The areas of these triangles are fairly comparable to the ones of the hexagons formed by the 5 mg/mL preparation. However, we observed that the nanoplates' heights decreased significantly, thus indicating that the decrease on material concentration affects the crystalline growth in a direction perpendicular to the substrate. This fact was also observed when decreasing the solution concentration from 10 to 5 mg/mL. Furthermore, the angles at the triangles' vertices were estimated to have a mean value of $(62 \pm 6)^\circ$. The top surfaces of the nanoplates revealed further details. In Figures 5g and 5i the existence of a collection of randomly oriented steps, emerging from a spiral core, generally located close to the center of these bidimensional features is observed. These cores qualitatively resemble the ones observed at higher concentration samples; however, in this present case they span a smaller area, until giving rise to the development of the random steps covering the rest of the nanoplates' surface. The height profiles of these structures are shown in Figures 6e and 6f. Starting with Figure 6e, from left to right, it is observed the edge of the nanoplate having a height close to 15 nm, while on its top the height of the randomly oriented steps has a value of $2.5 \pm 0.5 \text{ nm}$, while the lateral profile of one core (Figure 6f) is showed to be made out of the steps with heights around $3 \pm 1 \text{ nm}$.

The X-ray diffraction pattern of this sample is presented in Figure 7c. As for the previous samples, several diffraction peaks are observed and the maxima positions have been summarized in table 3. In most of the cases, the 1 mg/mL sXRD peaks are located at q -values comparable to the previous samples, thus suggesting that the triangular motifs could be formed by crystalline units consisting of upright standing molecules on the substrate, as before. We recall that the monoclinic unit cell obtained from the single crystal X-ray diffraction is composed of 2 molecules along the a axis; however the length of the almost linear organic molecule is comparable to half the d_{100} distance, *i. e.* about 2.7 nm. This value is fairly close to the one found for the steps on the nanoplates' surfaces formed by the 1 mg/mL deposition.

As the solution concentration was further decreased to 0.25 mg/mL, the triangular-shaped nanoplates were further evidenced, as observed by the AFM height images in Figures 5j, 5k and 5l. As in the previous case, these features span areas close to $5 \mu\text{m}^2$ and heights around 15 nm. Regarding their morphology, we observe standalone structures more organized towards achieving a “*perfect*” equilateral triangle. Figure 5k shows the AFM image of an individual triangle, almost equilateral with a mean value of $(60 \pm 2)^\circ$ for its inner angles. This fact has been observed in several nanoplates at this concentration. Also, a closer inspection at the right edge of this motif, showed that the final structure could be formed by the coalescence of 3 individual triangles, during crystal growth (see right edge). In comparison to nanoplates formed at higher concentrations, the top surfaces of these triangles have no topographic features, as observed by the height profile presented in Figure 6g; in other words, these triangles are almost flat on their tops (roughness about 0.3 nm). However, in some cases a layered structure was also observed, as the one presented in Figure 5l. The surface of the triangle shows a step-like disposition, possibly indicating the vestige of the molecule during crystal growth. In figure 6g, from left to right, it is possible to observe how the crystal edge develops from the surface up to a 15 nm height, then, on the nanoplate top surface, two steps are observed, each one of about 2.5 ± 0.5 nm height (Figure 6h). The change in the morphology, from hexagonal nanoplates to triangular structures could be related to a different crystal arrangement of the molecules (*i.e.* a new polymorph).

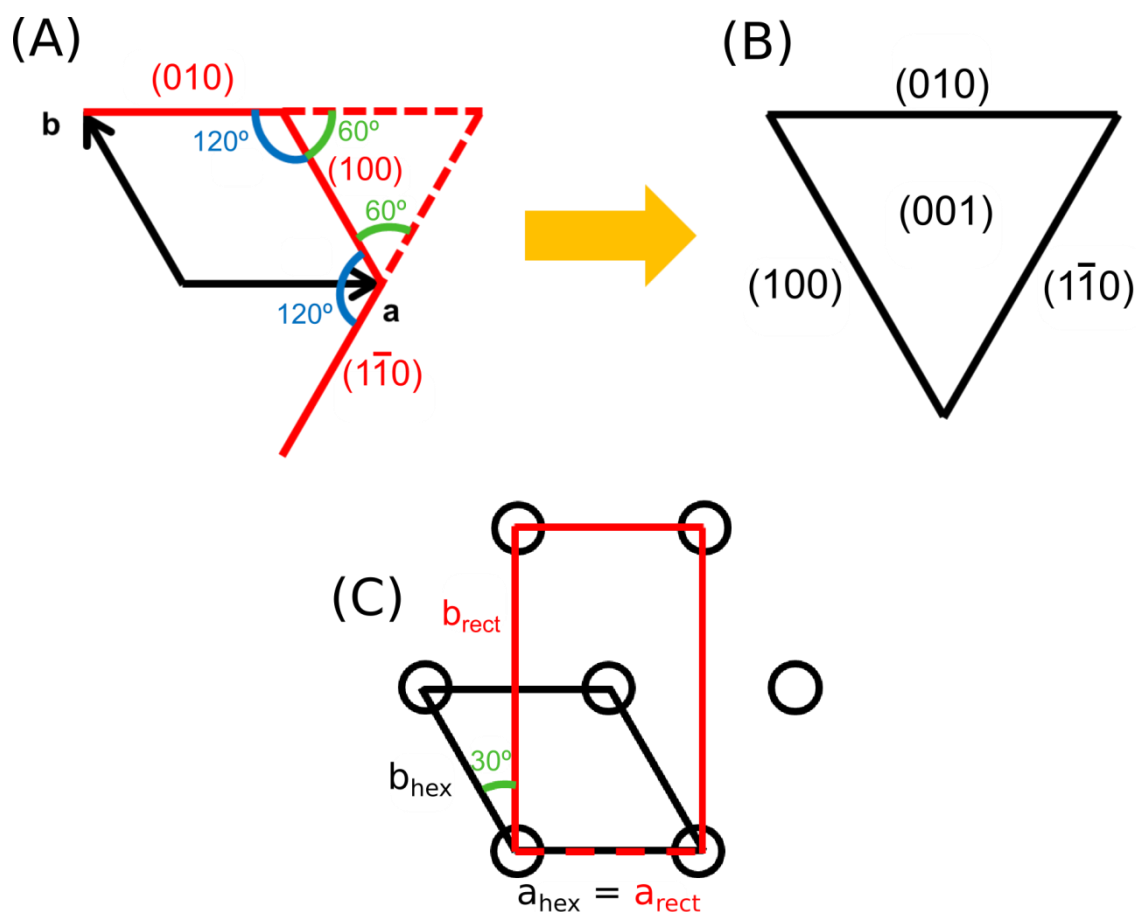


Figure 8. Scheme of the morphological change, as induced by a polymorphic transition from a monoclinic to a hexagonal phase: (a) proposed indexation of the faces of the triangular crystals from a hexagonal lattice viewed down the c axis (molecular long axis is supposed parallel to c axis). (b) Assumed crystal morphology. (c) Schematic representation of an hexagonal unit cell in the (a,b) plane together with the centered rectangular cell that can be built from it.

Taking into consideration the triangular-shaped morphology observed, it is possible to obtain it from a system that organizes in bulk in a hexagonal crystal lattice, as previously reported in the literature.³⁹⁻⁴² If we consider that the long molecular axis should be parallel to the c axis, the area of the $\{001\}$ faces should be the highest as for the bulk structure. Then, it can be envisaged that the low Miller indexes hexagonal $\{100\}$ faces (comprising (100) , (010) and $(1-10)$ as shown in Figure 8) should also cover a significant surface area, then resulting in a triangular shape (with all angles at 60°) as schematized in Figures 8a and 8b. Moreover, when viewed along the long axis a , the monoclinic bulk structure of this fluorinated molecule shows a packing similar to a centered rectangular unit cell. It is known that for discotic liquid crystals a two-dimensional centered rectangular cell can transform into a hexagonal cell by deformation of the rectangular cell.⁴³ This transformation is facilitated when $b_{\text{rect}}/a_{\text{rect}}$ is close to $\sqrt{3}$ as shown in Figure 8c (a_{rect} and b_{rect} are the unit cell dimensions of the

centered rectangular cell). From the known bulk structure of $F_{13}C_6$ -BTBT- C_6F_{13} it is possible to calculate⁴⁴ that $c/b = 1.543$, that is, a 11% difference from $\sqrt{3}$ thus evidencing that a transition from a monoclinic to a hexagonal phase, when solvent-solute interactions increase, can then be envisaged. Using the Celref software,⁴⁵ we have found a solution of unit cell parameters of a hexagonal crystalline phase that fit well with the positions of the reflections observed for the 1 mg/mL sample, as summarized in table 3. The quantitative values of the unit cell parameters are $a = 5.44 \pm 0.05 \text{ \AA}$, $c = 26.78 \pm 0.02 \text{ \AA}$, $V = 690 \pm 10 \text{ \AA}^3$, where the density of this proposed unit cell is consistent with those of the bulk phase. Thus, the triangular shaped crystals are formed by the transformation from the monoclinic unit cell towards a hexagonal unit cell of about half the size along the molecular axis. The formation of triangular nanometric features has been discussed previously in the literature in inorganic and organic systems.^{16, 39-42, 46-49} Taking into consideration organic nanoplates prepared from solution, Algra et al. on alizarin crystals¹⁶ found that the growth of triangular structures was dependent on the solvent used during deposition; specifically, when alcohol solutions were used, a part of the alizarin was deprotonated at one of the two hydroxyl groups in the molecule. Thus, it was suggested that this state somehow blocked the growth of the top and bottom and several side faces of the alizarin crystals resulting in a triangular morphology.¹⁶ Nonetheless, authors did not find the formation of a new polymorph, as in our present work. It is then possible that in our case, when the solution concentration is decreased, the solvent/molecule interaction increases due to the imminent material depletion, up to a point where nucleation and growth of a new crystal arrangement is triggered, accompanied by a morphological change of the nanoplates.

Conclusions

Nanoplates of the π -conjugated organic molecule 2,7-Diperfluorohexyl-[1]benzothieno[3,2,b]benzothiophene were prepared by a fast precipitation process. We found that by varying the solution parameters it was possible to tune the crystalline morphology of the nanometric features. At high concentrations, hexagonal motifs, with the same crystalline structure as the one of the bulk, were found. Then, as solution concentration was decreased, these motifs evolved toward forming triangular nanoplates. A detailed inspection by AFM supported by sXRD measurements allowed to determine that these triangles are composed of a new crystalline phase where only one molecule per unit cell is present as compared to four for the monoclinic structure.

Acknowledgments

The authors acknowledge financial support from the ARC program of the Communauté Française de Belgique (Grant No. 20061). This work has also been financially supported by the Walloon Region (WCS project N°1117306), and by the Belgian National Fund for Scientific Research (FNRS, POLYGRAD project N°22333186). Y. G. benefits from a mandate of Francqui Research Professor. B.C is a FNRS Research Fellow. G. S. kindly acknowledges postdoctoral fellowship support from the Wiener-Anspach Foundation.

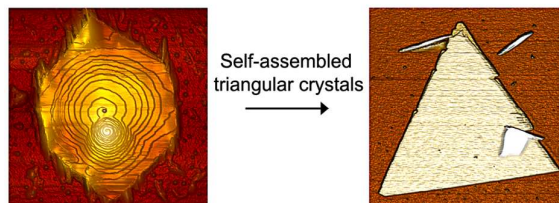
References

1. O. Werzer, N. Boucher, J. P. de Silva, G. Gbabode, Y. H. Geerts, O. Konovalov, A. Moser, J. Novak, R. Resel and M. Sferrazza, *Langmuir*, 2012, **28**, 8530-8536.
2. G. Gbabode, M. Dohr, C. Niebel, J.-Y. Balandier, C. Ruzié, P. Négrier, D. Mondieig, Y. H. Geerts, R. Resel and M. Sferrazza, *ACS Applied Materials & Interfaces*, 2014, **6**, 13413-13421.
3. A. O. F. Jones, Y. H. Geerts, J. Karpinska, A. R. Kennedy, R. Resel, C. Röthel, C. Ruzié, O. Werzer and M. Sferrazza, *ACS Applied Materials & Interfaces*, 2015, **7**, 1868-1873.
4. F. Dinelli, M. Murgia, P. Levy, M. Cavallini, F. Biscarini and D. M. de Leeuw, *Physical Review Letters*, 2004, **92**, 116802.
5. A. Shehu, S. D. Quiroga, P. D'Angelo, C. Albonetti, F. Borgatti, M. Murgia, A. Scorzoni, P. Stoliar and F. Biscarini, *Physical Review Letters*, 2010, **104**, 246602.
6. X. Zhuang, Y. Mai, D. Wu, F. Zhang and X. Feng, *Advanced Materials*, 2015, **27**, 403-427.
7. G. Gbabode, N. Dumont, F. Quist, G. Schweicher, A. Moser, P. Viville, R. Lazzaroni and Y. H. Geerts, *Advanced Materials*, 2012, **24**, 658-662.
8. C. Lercher, R. Resel, J.-Y. Balandier, C. Niebel, Y. H. Geerts, M. Sferrazza and G. Gbabode, *Journal of Crystal Growth*, 2014, **386**, 128-134.
9. G. Gbabode and B. Chattopadhyay, in *Non-equilibrium Phenomena in Confined Soft Matter*, ed. S. Napolitano, Springer, 2015.
10. S. A. Morin, A. Forticaux, M. J. Bierman and S. Jin, *Nano Letters*, 2011, **11**, 4449-4455.
11. X. Bai, L. Zheng, N. Li, B. Dong and H. Liu, *Crystal Growth & Design*, 2008, **8**, 3840-3846.
12. A. Gupta, T. Sakthivel and S. Seal, *Progress in Materials Science*, 2015, **73**, 44-126.
13. C. He, D. Wu, F. Zhang, M. Xue, X. Zhuang, F. Qiu and X. Feng, *ChemPhysChem*, 2013, **14**, 2954-2960.
14. Q. An, Q. Chen, W. Zhu, Y. Li, C.-a. Tao, H. Yang, Z. Li, L. Wan, H. Tian and G. Li, *Chemical Communications*, 2010, **46**, 725-727.
15. H. Liu, X. Cao, Y. Wu, Q. Liao, A. J. Jimenez, F. Wurthner and H. Fu, *Chemical Communications*, 2014, **50**, 4620-4623.
16. R. E. Algra, W. S. Graswinckel, W. J. P. v. Enckevort and E. Vlieg, *Journal of Crystal Growth*, 2005, **285**, 168-177.
17. A. Facchetti, *Materials Today*, 2007, **10**, 28-37.
18. Y. V. Zherdeva, A. Barudi, A. Y. Zheltov and B. I. Stepanov, *J. Org. Chem. USSR*, 1980, **16**, 383.
19. G. Sheldrick, *Acta Crystallographica Section A*, 2008, **64**, 112-122.
20. M. A. Spackman and D. Jayatilaka, *CrystEngComm*, 2009, **11**, 19-32.
21. M. A. Spackman, *Physica Scripta*, 2013, **87**, 048103.
22. M. A. Spackman and J. J. McKinnon, *CrystEngComm*, 2002, **4**, 378-392.
23. S. K. Wolff, D. J. Grimwood, J. J. McKinnon, M. J. Turner, D. Jayatilaka and M. A. Spackman, *Journal*, 2012.
24. P. Hartman and P. Bennema, *J. Cryst. Growth*, 1980, **49**, 145-156.
25. R. Docherty, G. Clydesdale, K. J. Roberts and P. Bennema, *J. Phys. D: Appl. Phys.*, 1991, **24**, 89-99.
26. M. A. Lovette, A. R. Browning, D. W. Griffin, J. P. Sizemore, R. C. Snyder and M. F. Doherty, *Ind. Eng. Chem. Res.*, 2008, **47**, 9812-9833.
27. H. Sun, *J. Phys. Chem. B*, 1998, **102**, 7338-7364.
28. T. Izawa, E. Miyazaki and K. Takimiya, *Advanced Materials*, 2008, **20**, 3388-3392.
29. C. Niebel, Y. Kim, C. Ruzie, J. Karpinska, B. Chattopadhyay, G. Schweicher, A. Richard, V. Lemaury, Y. Olivier, J. Cornil, A. R. Kennedy, Y. Diaoy, W.-Y. Lee, S. Mannsfeld, Z. Bao and Y. H. Geerts, *Journal of Materials Chemistry C*, 2015, **3**, 674-685.
30. Please beware that {hkl} written between brackets correspond to all related faces of the given hkl face according to the monoclinic symmetry, that is, hkl, h-kl, -hk-l and -h-k-l
31. C. M. Pina, U. Becker, P. Risthaus, D. Bosbach and A. Putnis, *Nature*, 1998, **395**, 483-486.
32. R. E. Sours, A. Z. Zellelow and J. A. Swift, *The Journal of Physical Chemistry B*, 2005, **109**, 9989-9995.
33. A. Dhotel, L. Delbreilh, B. Youssef, J. Jiang, G. Coquerel, J.-M. Saiter and L. Tan, *J Therm Anal Calorim*, 2013, **112**, 301-305.
34. W. K. Burton, N. Cabrera and F. C. Frank, *The Growth of Crystals and the Equilibrium Structure of their Surfaces*, 1951.
35. E. I. Givargizov, *Oriented Crystallization on Amorphous Substrates*, Springer Science, 1991.
36. F. C. Frank, *Discussions of the Faraday Society*, 1949, **5**, 48-54.
- 37.

38. P. M. Martins and F. Rocha, *Surface Science*, 2007, **601**, 3400-3408.
39. N. Pinna, K. Weiss, J. Urban and M. P. Pileni, *Advanced Materials*, 2001, **13**, 261-264.
40. T. Kuykendall, P. Pauzauskie, S. Lee, Y. Zhang, J. Goldberger and P. Yang, *Nano Letters*, 2003, **3**, 1063-1066.
41. A. Courty, A. I. Henry, N. Goubet and M. P. Pileni, *Nat Mater*, 2007, **6**, 900-907.
42. H. R. Gutiérrez, N. Perea-López, A. L. Elías, A. Berkdemir, B. Wang, R. Lv, F. López-Urías, V. H. Crespi, H. Terrones and M. Terrones, *Nano Letters*, 2013, **13**, 3447-3454.
43. G. Schweicher, G. Gbabode, F. Quist, O. Debever, N. Dumont, S. Sergeev and Y. H. Geerts, *Chemistry of Materials*, 2009, **21**, 5867-5874.
44. In the present lattice c would correspond to b_{rect} and b to a_{rect} when comparing to the figure presented at the previous slide
45. J. Laugier and B. Bochu, <http://www.ccp14.ac.uk/solution/unitcellrefine/>, 2003.
46. L. Cartier, T. Okihara and B. Lotz, *Macromolecules*, 1997, **30**, 6313-6322.
47. L. Cartier and B. Lotz, *Macromolecules*, 1998, **31**, 3049-3054.
48. A. I. Henry, A. Courty, N. Goubet and M. P. Pileni, *The Journal of Physical Chemistry C*, 2008, **112**, 48-52.
49. J. E. Millstone, D. G. Georganopoulou, X. Xu, W. Wei, S. Li and C. A. Mirkin, *Small*, 2008, **4**, 2176-2180.

Table of contents entry**Self-assembled π -conjugated organic nanoplates: from hexagonal to triangular motifs.**

Daniel E. Martínez-Tong, Gabin Gbabwe, Christian Ruzié, Basab Chattopadhyay, Guillaume Schweicher, Alan R. Kennedy, Yves H. Geerts, Michele Sferrazza



The formation of triangular nanoplates of an organic semiconducting compound is discussed by considering enhanced solvent/molecule interactions.

Keywords: Self-assembled Nanostructures; Triangular nanoplates; Polymorphism; Organic semiconducting molecules